Theoret. Comput. Fluid Dynamics (2004) 18: 251–263
Digital Object Identifier (DOI) 10.1007/s00162-004-0132-6

**Theoretical and Computational Fluid Dynamics**

*Original article*

# Hydromagnetic convection in a rotating annulus with an azimuthal magnetic field[*]

E. Kurt, F.H. Busse, W. Pesch

Institute of Physics, University of Bayreuth, 95440 Bayreuth, Germany

Received September 29, 2003 / Accepted May 25, 2004

Communicated by H.J.S. Fernando

**Abstract.** The problem of convection induced by radial buoyancy in an electrically conducting fluid contained by a rotating cylindrical annulus (angular frequency, $\Omega$) in the presence of a homogeneous magnetic field ($B$) in the azimuthal direction is considered. The small gap approximation is used together with rigid cylindrical boundaries. The onset of convection occurs in the form of axial, axisymmetric or oblique rolls. The angle $\psi$ between the roll axis and the axis of rotation depends of the ratio between the Chandrasekhar number, $Q \sim B^2$, and the Coriolis number, $\tau \sim \Omega$. Fully three-dimensional numerical simulations as well as Galerkin representations for roll patterns including the subsequent stability analysis are used in the theoretical investigation. At finite amplitudes, secondary transitions to 3D-hexarolls and to spatio-temporal chaos are found. Overlapping regions of pattern stability exist such that the asymptotically realized state may depend on the initial conditions.

**Key words:** convection, magnetic field, rotating annulus, stability
**PACS:** 47.27.-i, 47.65.+a

## 1 Introduction

Convection driven by thermal buoyancy in rotating fluid layers heated from below in the presence of a magnetic field is a typical problem encountered in planetary and stellar fluid dynamics. The most commonly treated version of this problem corresponds to the case when both, the axis of rotation and the direction of the imposed homogenous magnetic field, are parallel to the gravity vector. The onset of convection in this case was considered by Chandrasekhar [6]. He found the surprising result that the Lorentz force and the Coriolis force may counter each other such that the critical Rayleigh number for onset of convection is lower than in cases when either the magnetic field or the rotation rate vanishes.

For planetary and stellar applications the configuration of rotation axis and magnetic field direction perpendicular to each other and perpendicular to the gravity vector could be more important. It corresponds to the case of convection in the equatorial regions of rotating spherical fluid shells when an azimuthal magnetic field is imposed. Toroidal magnetic fields in the electrically conducting cores of planets or in the solar atmosphere are believed to be often much stronger than the poloidal components which can be measured from the

---

*Correspondence to:* E. Kurt (e-mail: Erol.Kurt@uni-bayreuth.de)

[*] The authors gratefully acknowledge the support from the European Graduate College, under Grant No: GRK 698/1.

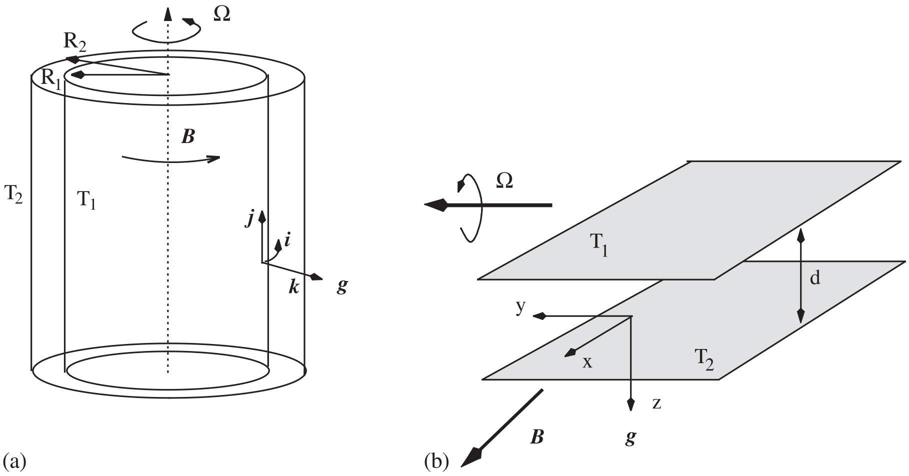

**Fig. 1.** (**a**) Schematic representation of the rotating annulus. (**b**) The analogy to the planar convection ($d \equiv R_2 - R_1$)

outside. It is thus of interest to study the properties of convection in this situation which can also be realized in laboratory experiments through the use of the rotating annulus configuration (see Fig. 1a). In this case the centrifugal force is used as effective gravity and the radial direction thus corresponds to "vertical". Although the motivation for the rotating magnetic annulus experiment has arisen in the geophysical context, the problem is also of interest from a more general point of view in that it concerned with formations of patterns in the presence of two competing directional effects. In fact, as will be demonstrated a large variety of convection patterns is found already at small values of the rotation and magnetic field parameters for moderate values of the Rayleigh number. In this respect the present paper can be regarded as an extension of the paper by Auer et al. [2] to the case when a homogeneous magnetic field is added. A rotating annulus experiment corresponding to the paper of Auer et al. [2] has been performed by Jaletzky and Busse [9].

In Sect. 2 the mathematical formulation of the problem is discussed and an outline of the computational procedures is given. In the small gap approximation, the problem reduces to the case of a horizontal fluid layer heated from below with magnetic field, axis of rotation, and the vertical direction corresponding to the $x$-, $y$- and $z$-axis of a Cartesian system of coordinates. A sketch of the geometrical configuration to be considered in this paper is shown in Fig. 1b.

The results of the linear theory for the onset of convection which has first been considered by Eltayeb [7] more than 30 years ago are discussed in Sect. 3. In order to obtain simple expressions, Eltayeb has used idealized boundary conditions, namely stress-free conditions for the velocity field and electrically infinitely conducting boundaries for the magnetic field. In the present paper the more realistic case of rigid, electrically insulating boundaries is considered. The weakly nonlinear analysis and a stability analysis of convection rolls is described in Sect. 4. A survey of the various patterns of convection that are introduced by secondary bifurcations is given in Sect. 5. Some of the instabilities of convection rolls can be understood on the basis of analytical results obtained in earlier work on the related problem of convection in the absence of a magnetic field (Auer et al. [2], Busse et al. [4]). But new mechanisms of instability are introduced by the Lorentz force. Future research and potential application are discussed in the concluding section.

## 2 Mathematical formulation of the problem and numerical methods

In the following, we refer to the situation shown in Fig. 1b. The effective gravity is provided by the centrifugal force, $g = \Omega^2(R_1 + R_2)/2$, and its direction is given by the unit vector $\boldsymbol{k}$. The upper and lower boundaries are kept at the constant temperatures $T_1$ and $T_2$, $T_2 > T_1$, respectively. In this paper we use the thickness $d$ of the layer as length scale, the vertical diffusion time, $\frac{d^2}{\kappa} = t_\kappa$, as time scale, $(T_2 - T_1)/R$ as temperature scale, and the magnetic flux density $B_0$ of the imposed field as scale of the magnetic field. Then the basic equations of motion for the velocity field $\boldsymbol{u}$, the heat equation for the deviation $\Theta$ of the temperature from the state of pure conduction and the equation of magnetic induction in dimensionless form read as follows:

$$P^{-1}\left(\frac{\partial}{\partial t}+\boldsymbol{u}\cdot\nabla\right)\boldsymbol{u}+2\tau\boldsymbol{j}\times\boldsymbol{u}=-\nabla\Pi-\boldsymbol{k}\Theta+\nabla^2\boldsymbol{u}+Q\left(\boldsymbol{i}+\frac{\kappa}{\lambda}\boldsymbol{b}\right)\cdot\nabla\boldsymbol{b}, \tag{1a}$$

$$\nabla\cdot\boldsymbol{u}=0, \tag{1b}$$

$$\left(\frac{\partial}{\partial t}+\boldsymbol{u}\cdot\nabla\right)\Theta=-R\boldsymbol{k}\cdot\boldsymbol{u}+\nabla^2\Theta, \tag{1c}$$

$$\frac{\kappa}{\lambda}\left(\frac{\partial}{\partial t}\boldsymbol{b}+\boldsymbol{u}\cdot\nabla\boldsymbol{b}-\boldsymbol{b}\cdot\nabla\boldsymbol{u}\right)=\boldsymbol{i}\cdot\nabla\boldsymbol{u}+\nabla^2\boldsymbol{b}, \tag{1d}$$

$$\nabla\cdot\boldsymbol{b}=0, \tag{1e}$$

where all gradient terms in Eq. (1a) have been combined into the pressure term $\nabla\Pi$. The Rayleigh number $R$, the Prandtl number $P$, the Coriolis parameter $\tau$ and the Chandrasekhar number $Q$ are defined by

$$R=\left(\alpha(T_2-T_1)gd^3\right)/(\nu\kappa),\quad P=\frac{\nu}{\kappa},\quad \tau=\Omega d^2/\nu,\quad Q=\left(B_0{}^2d^2\right)/(\varrho\mu\lambda\nu), \tag{2}$$

where $\alpha$, $\nu$, $\kappa$, $\mu$ and $\lambda$ are the coefficient of thermal expansion, the kinematic viscosity, the thermal diffusivity, the magnetic permeability and the magnetic diffusivity of the fluid, respectively. The magnetic field has been represented in the form $\boldsymbol{B}=B_o(\boldsymbol{i}+\frac{\kappa}{\lambda}\boldsymbol{b})$ where $\boldsymbol{i}$ is the unit vector in the $x$-direction. In the following we shall focus the attention on the case of liquid metals where $\frac{\kappa}{\lambda}$ is of the order $10^{-4}$ to $10^{-5}$. Hence we shall adopt in this paper the limit $\kappa\ll\lambda$ and drop the terms on the left hand side of Eq. (1d) and the term multiplied by $\frac{\kappa}{\lambda}$ in Eq. (1a).

We use a Cartesian system of coordinates with the unit vectors $\boldsymbol{i}$, $\boldsymbol{j}$, $\boldsymbol{k}$ in the direction of the $x$, $y$, $z$-axes as shown in Fig. 1. The conditions at the boundaries are then given by

$$\boldsymbol{u}=0,\quad \Theta=0,\quad \nabla\times\boldsymbol{b}\cdot\boldsymbol{k}=0 \text{ at } z=\pm\frac{1}{2}. \tag{3}$$

The continuity of the magnetic field $\boldsymbol{b}$ across the boundaries does not have to be taken into account explicitly in the limit $\kappa\ll\lambda$ as will be pointed out below. Following earlier papers (Auer et al. [2], Busse et al. [4]) we assume periodic boundary conditions in the $x$, $y$-plane. The agreement between the results of those papers and the experimental observations of Jaletzky and Busse [9] indicates that the periodic boundary conditions as well as the small gap approximation are appropriate for the rotating annulus experiment at the moderate values of $\tau$ to be considered in this paper. In order to eliminate the pressure term in Eq. (1a) we introduce the general representations for the solenoidal vector fields $\boldsymbol{u}$ and $\boldsymbol{b}$, (see Eqs. (1b) and (1e)):

$$\boldsymbol{u}=\overline{\boldsymbol{u}}+\nabla\times(\nabla\times\boldsymbol{k}v)+\nabla\times\boldsymbol{k}w\equiv\overline{\boldsymbol{u}}+\boldsymbol{\delta}v+\boldsymbol{\varepsilon}w, \tag{4a}$$

$$\boldsymbol{b}=\overline{\boldsymbol{b}}+\nabla\times(\nabla\times\boldsymbol{k}h)+\nabla\times\boldsymbol{k}g\equiv\overline{\boldsymbol{b}}+\boldsymbol{\delta}h+\boldsymbol{\varepsilon}g, \tag{4b}$$

where overbars in $\overline{\boldsymbol{u}}$ and $\overline{\boldsymbol{b}}$ denote the average over the $x$, $y-$ plane of $\boldsymbol{u}$ and $\boldsymbol{b}$. The functions $v$, $h$ and $w$, $g$ describing the poloidal and toroidal components of the velocity and the magnetic field, respectively are uniquely defined if the conditions $\overline{v}=\overline{h}=\overline{w}=\overline{g}=0$ are imposed. After the application of the differential operators $\boldsymbol{\delta}$ and $\boldsymbol{\varepsilon}$ on the velocity Eq. (1a) we arrive at the following equations for $v$ and $w$

$$\nabla^4\Delta_2v-2\tau\frac{\partial}{\partial y}\Delta_2w+\Delta_2\theta+Q\boldsymbol{i}\cdot\nabla\nabla^2\Delta_2h=P^{-1}\left[\frac{\partial}{\partial t}\nabla^2\Delta_2v+\boldsymbol{\delta}\cdot(\boldsymbol{u}\cdot\nabla)\boldsymbol{u}\right], \tag{5a}$$

$$\nabla^2\Delta_2w+2\tau\frac{\partial}{\partial y}\Delta_2v+Q\boldsymbol{i}\cdot\nabla\Delta_2g=P^{-1}\left[\frac{\partial}{\partial t}\Delta_2w+\boldsymbol{\varepsilon}\cdot(\boldsymbol{u}\cdot\nabla)\boldsymbol{u}\right]. \tag{5b}$$

In addition, an equation for the mean flow $\overline{\boldsymbol{u}}$ is obtained by averaging the velocity Eq. (1a) over the $x$–$y$ plane.

$$\frac{\partial^2}{\partial z^2}\overline{\boldsymbol{u}}=\frac{1}{P}\left(\frac{\partial}{\partial t}\overline{\boldsymbol{u}}-\frac{\partial}{\partial z}\overline{\Delta_2v\left(\nabla_2\frac{\partial}{\partial z}v+\boldsymbol{\varepsilon}w\right)}\right). \tag{6}$$

Analogously, when applying $\boldsymbol{\delta}$ and $\boldsymbol{\varepsilon}$ on Eq. (1d), we obtain in the limit $\frac{\kappa}{\lambda} \to 0$

$$\nabla^2 \Delta_2 h = -\boldsymbol{i} \cdot \nabla \Delta_2 v, \tag{7a}$$

$$\nabla^2 \Delta_2 g = -\boldsymbol{i} \cdot \nabla \Delta_2 w. \tag{7b}$$

The heat equation (1c) can now be written in the form

$$\nabla^2 \Theta + R \Delta_2 v = (\boldsymbol{\delta} v + \boldsymbol{\varepsilon} w + \overline{\boldsymbol{u}}) \cdot \nabla \Theta + \frac{\partial}{\partial t} \Theta. \tag{8}$$

The mean distortion $\overline{\boldsymbol{b}}$ of the magnetic field does not enter the problem since it vanishes in the limit $\kappa \ll \lambda$. In writing Eqs. (5–8) we have introduced the *horizontal gradient*, $\nabla_2 \equiv \nabla - \boldsymbol{kk} \cdot \nabla$, and the horizontal Laplacian, $\Delta_2 \equiv \nabla_2 \cdot \nabla_2$. In line with Eqs. (3,4) the basic Eqs. (5–8) must be solved subject to the boundary conditions

$$v = \frac{\partial}{\partial z} v = w = \Theta = g = 0 \text{ at } z = \pm \frac{1}{2}. \tag{9}$$

The Eq. (7a) for $h$ and the corresponding boundary condition can be dropped, since $h$ can be eliminated from the problem by replacing $\nabla^2 \Delta_2 h$ in Eq. (5a) with $\boldsymbol{i} \cdot \nabla \Delta_2 v$ in accordance with Eq. (7a). As usual we assume the idealization of an infinitely extended fluid layer in the horizontal plane, i.e., the $x$, $y$- dependence is captured by a $2D$ Fourier series.

For simplicity, a symbolic notation for the Eqs. (5-8) is used in the following

$$\mathcal{C} \frac{d}{dt} \boldsymbol{V}(\boldsymbol{x}, t) = \mathcal{L} \boldsymbol{V}(\boldsymbol{x}, t) + \boldsymbol{N}(\boldsymbol{V}(\boldsymbol{x}, t) | \boldsymbol{V}(\boldsymbol{x}, t)), \; \mathcal{L} = \mathcal{A} + R\, \mathcal{B}, \tag{10}$$

where the symbolic vector $\boldsymbol{V}(\boldsymbol{x}, t) = (v, w, g, \Theta, \overline{\boldsymbol{u}})$ represents the fields in Eqs. (5–8). $\boldsymbol{V}(\boldsymbol{x}, t) \equiv 0$ corresponds to the ground state. The operators $\mathcal{C}$, $\mathcal{L}$, $\mathcal{A}$ and $\mathcal{B}$ are linear differential operators while $\boldsymbol{N}$ describes the quadratic nonlinearities. Note that we have made explicit the Rayleigh number, $R$, in the definition $\mathcal{L} = \mathcal{A} + R\, \mathcal{B}$ of the linear operator $\mathcal{L}$.

To describe the solution periodic in the plane of the problem posed by Eq. (5) through Eq. (8) and the boundary conditions (9) we use the Galerkin method. The boundary conditions (9) are satisfied by expansions in suitable complete sets of functions:

$$v(x, y, z, t) = \sum_{n=1}^{N} \sum_{l,m=-M}^{M} v_{lmn}(t) \exp\left[i(lq_x x + mq_y y)\right] f_n(z), \tag{11a}$$

$$w(x, y, z, t) = \sum_{n=1}^{N} \sum_{l,m=-M}^{M} w_{lmn}(t) \exp\left[i(lq_x x + mq_y y)\right] \sin n\pi \left(z + \frac{1}{2}\right), \tag{11b}$$

$$g(x, y, z, t) = \sum_{n=1}^{N} \sum_{l,m=-M}^{M} g_{lmn}(t) \exp\left[i(lq_x x + mq_y y)\right] \sin n\pi \left(z + \frac{1}{2}\right), \tag{11c}$$

$$\Theta(x, y, z, t) = \sum_{n=1}^{N} \sum_{l,m=-M}^{M} \Theta_{lmn}(t) \exp\left[i(lq_x x + mq_y y)\right] \sin n\pi \left(z + \frac{1}{2}\right), \tag{11d}$$

$$\overline{\boldsymbol{u}}(z, t) = \sum_{n=1}^{N} \boldsymbol{u}_n(t) \sin n\pi \left(z + \frac{1}{2}\right). \tag{11e}$$

The $f_n(z)$ denotes the Chandrasekhar functions (Chandrasekhar [6]) $f_n\left(\pm\frac{1}{2}\right) = \frac{\partial}{\partial z} f_n\left(\pm\frac{1}{2}\right) = 0$,

$$f_n(z) = \begin{cases} \dfrac{\cosh \beta_n z}{\cosh \beta_n/2} - \dfrac{\cos \beta_n z}{\cos \beta_n/2} & \text{for odd } n, \\ \dfrac{\sinh \beta_n z}{\sinh \beta_n/2} - \dfrac{\sin \beta_n z}{\sin \beta_n/2} & \text{for even } n. \end{cases} \tag{12}$$

The coefficients $\beta_n$ are determined as roots of the equations,

$$\tanh \beta_n/2 + \tan \beta_n/2 = 0 \text{ for odd } n, \quad \coth \beta_n/2 - \cot \beta_n/2 = 0 \text{ for even } n. \tag{13}$$

The summation in the velocity expressions (11a–c) runs through all positive integers $n$ and through all integers $l$ and $m$ with the exception of the case $l = m = 0$ in the sums (11a–c). In the sum (11d) the terms $l = m = 0$ must be included since they describe the distortion of the mean temperature profile. The reality of all fields requires $v_{l,m,n} = v^*{}_{-l,-m,n}$, etc., where the star indicates the complex conjugate.

The expressions (11) are inserted into Eqs. (5,7,8) and projected onto the various expansion functions in Eq. (11). Thus, one obtains a set of ordinary nonlinear differential equations for the coefficients $a_{lmn}(t)$, $b_{lmn}(t)$, $c_{lmn}(t)$ and $\boldsymbol{u}_n(t)$. Since the coefficients $g_{lmn}(t)$ are slaved to the $w_{lmn}(t)$ according to Eq. (7b) as:

$$g_{lmn}(t) = \frac{i\, l\, q_x\, w_{lmn}(t)}{l^2 {q_x}^2 + m^2 {q_y}^2 + n^2 \pi^2}, \tag{14}$$

they can be eliminated from the beginning.

The sums (11) will describe the solution correctly only in the limit when the parameters $N$ and $M$ tend to infinity. But in order to actually solve the infinite system for the expansion coefficients, finite values of $N$ and $M$ must be adopted. We are interested in solutions for moderate Rayleigh number and find that typically truncation parameters $M = 4$ and $N = 4$ have been sufficient to achieve an accuracy of about 1% in the Galerkin approach for periodic solutions. To check the accuracy of these solutions the truncation parameters have been increased to $M = N = 6$ in some cases. In order to assess complex spatio-temporal solutions in a large horizontal domain and also to validate the Galerkin results, we have performed direct simulations of the basic Eqs. (1) as well using typically the truncation parameters $M = 64$ and $N = 4$. For this purpose we have adopted a well proven code originally designed for ordinary Rayleigh–Bénard (RB) convection (Pesch [10]). The code uses in principle the Galerkin representation (11) and solves the horizontal dependence with a pseudo-spectral method. The time stepping is implicit with respect to the linear parts and explicit (Adams–Bashforth) with respect to the nonlinear parts. In special cases simulations with $M = 128$ and $N = 4$ have been carried out.

## 3 Linear analysis for the onset of convection

In order to determine the neutral curve for instability of the ground state $\boldsymbol{V}(\boldsymbol{x}, t) \equiv 0$ we use the ansatz

$$\boldsymbol{V}(\boldsymbol{x}, t) = \exp\left[\sigma t + i\boldsymbol{q} \cdot \boldsymbol{x}\right] \boldsymbol{V}_{lin}(\boldsymbol{q}, z) \tag{15}$$

in Eq. (10) which leads to the linear eigenvalue problem

$$\sigma(\boldsymbol{q}, R) \mathcal{C} \boldsymbol{V}_{lin}(\boldsymbol{q}, z) = (\mathcal{A} + R\, \mathcal{B}) \boldsymbol{V}_{lin}(\boldsymbol{q}, z) \tag{16}$$

where we have introduced the wavevector $\boldsymbol{q} = (q_x, q_y, 0)$. The condition that the maximum real part of $\sigma$ vanishes, $\Re\{\sigma(\boldsymbol{q}, R)\} = 0$, determines the neutral curve, $R = R_0(\boldsymbol{q})$. The minimum of $R_0(\boldsymbol{q})$ with respect to $\boldsymbol{q}$ yields the critical wave vector $\boldsymbol{q}_c$. Thus the critical Rayleigh number $R_c$ satisfies $R_c = R_0(\boldsymbol{q}_c)$.

We have found that the onset of convection is always stationary, in which case $\Im\{\sigma(\boldsymbol{q}, R_0)\} = 0$ holds as well, in accordance with the findings of Eltayeb [8] in the limit $\kappa \ll \lambda$. The neutral curve can thus be obtained more simply as the smallest eigenvalue $R = R_0(\boldsymbol{q})$ of the linear eigenvalue problem ($\sigma = 0$ in Eq. (16))

$$(\mathcal{A} + R\, \mathcal{B}) \boldsymbol{V}_{lin}(\boldsymbol{q}, z) = 0. \tag{17}$$

Note that the stationary threshold does not depend on the Prandtl number $P$. In the framework of our Galerkin ansatz the operators $\mathcal{A}$, $\mathcal{B}$ are mapped on matrices. For the resulting eigenvalue problem effective computer routines are available. This approach also facilitates the subsequent weakly nonlinear analysis.

A very useful analytical approximation of $R_0(\boldsymbol{q})$ as a function of control parameters $\tau$ and $Q$ is obtained if only one $z$ mode is retained in (11), i.e. $(N=1)$,

$$R_0(\boldsymbol{q}) = R^{RB}(|\boldsymbol{q}|) + \frac{4\,\tau^2\left(\boldsymbol{q}^2+\pi^2\right)^2 \sin^2\psi}{\left(\boldsymbol{q}^2+\pi^2\right)^2 + Q\,\boldsymbol{q}^2\cos^2\psi} + c_1\,Q\left(\boldsymbol{q}^2+\pi^2\right)\cos^2\psi, \tag{18a}$$

$$R^{RB}(|\boldsymbol{q}|) = \frac{\left(\boldsymbol{q}^4+2\,\pi^2\,c_2\,\boldsymbol{q}^2+\pi^4\,c_3\right)\left(\boldsymbol{q}^2+\pi^2\right)c_1}{\boldsymbol{q}^2}. \tag{18b}$$

Here, $\boldsymbol{q}=(q_x,q_y)$ is the wave vector of the rolls and the obliqueness angle $\psi \sim \arctan\frac{q_y}{q_x}$ thus denotes the angle between the rolls and the rotation axis. The numerical constants $c_1$, $c_2$, $c_3$ are combinations of certain overlap integrals of trigonometric and Chandrasekhar functions (12) and assume the values $c_1=1.0281$, $c_2=1.2465$ and $c_3=5.1388$. Note that Eq. (18a) is exact for free boundary conditions where $c_i=1$ for $i=1,2,3$ holds. The minimum of $R^{RB}(|\boldsymbol{q}|)$ yields an approximate Rayleigh–Bénard (RB) threshold $(\tau=Q=0)$ with $|\boldsymbol{q}|_c=3.0963$, $R^{RB}=1728.38$. The well-known rigorous values $|\boldsymbol{q}|_c=3.116$ and $R^{RB}=1707.76$ differ by less then 1.2% from the approximate ones.

From Eq. (18a) it is obvious that in the case $\tau \gg Q$ the minimum of $R_c(|\boldsymbol{q}|_c)$ is obtained for $\psi=0°$ ("axial rolls"). It is interesting that the relation

$$R_\tau(\boldsymbol{q}) = R^{RB}(|\boldsymbol{q}|) + 4\tau^2\sin^2\psi \tag{19}$$

which derives from Eq. (18a) for $Q=0$ is mathematically rigorous if the exact neutral curve $R^{RB}(|\boldsymbol{q}|)$ for Rayleigh–Bénard convection is chosen.

In the opposite limit, $Q \gg \tau$, the minimum of $R_0(\boldsymbol{q})$ is found at $\psi=90°$ ("zonal rolls"). In the intermediate regime $Q \sim \tau$ we have oblique rolls at onset $(0° < \psi < 90°)$, for instance, $\psi=55°$ for $Q=14$ and $\tau=8$.

The general numerical results for $R_c$ and $q_c$ as function of $\tau$ and $Q$ are shown in Fig. 2 and Fig. 3. The critical Rayleigh number, $R_c(\tau, Q)$ in Fig. 2a is always larger than $R^{RB}(\boldsymbol{q_c})$. It increases linearly at small $Q$ and quadratically at small $\tau$, in perfect agreement with the analytical approximation (18a). The modulus $q_c=|\boldsymbol{q_c}|$ of the critical wave vector shown in Fig. 2b decreases monotonously from the RB value $(q_c=3.116)$ to smaller values for increasing $\tau$ and $Q$.

The obliqueness angle $\psi$ as a function of $\tau$ and $Q$ is given in Fig. 3. One observes a transition from zonal rolls $(\psi=90°)$ to axial rolls $(\psi=0°)$ via intermediate oblique rolls with increasing $\tau$ at fixed $Q$. The transition lines between zonal rolls, oblique rolls and axial rolls in the $Q$–$\tau$ plane are shown in Fig. 3b. (See also the upper and lower faces of the parallelepiped in Fig. 3a.) Apparently, the oblique roll region is confined by an almost linear upper curve and an approximately parabolic lower curve as indicated in Fig. 3b.

In general the approximate values for $q_c$ and $R_c$ obtained from (18) deviate by less than 1% from the exact (numerical) ones (Fig. 2). For instance, for the parameter values $\tau=84$ and $Q=300$, we find

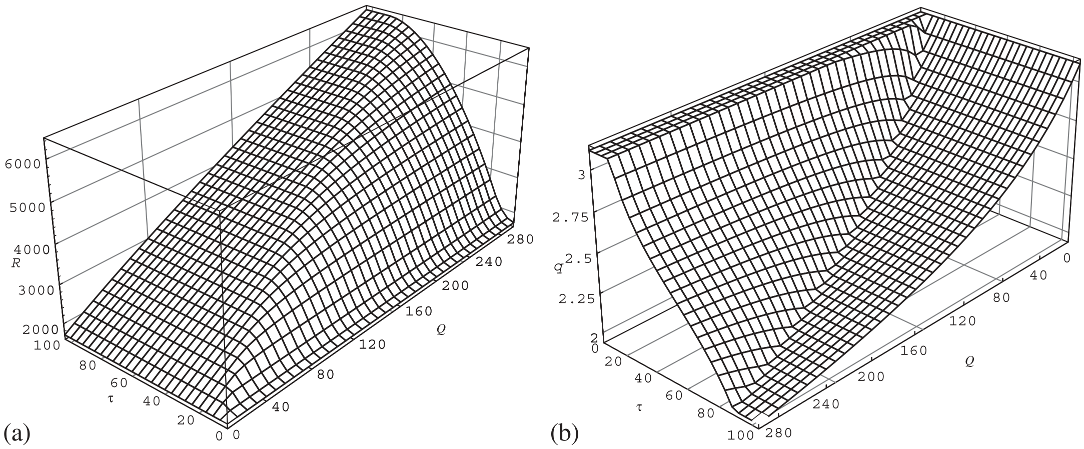

**Fig. 2.** (**a**) Critical Rayleigh numbers, $R_c$, (**b**) critical wave numbers, $q_c$, as a function of $\tau$ and $Q$

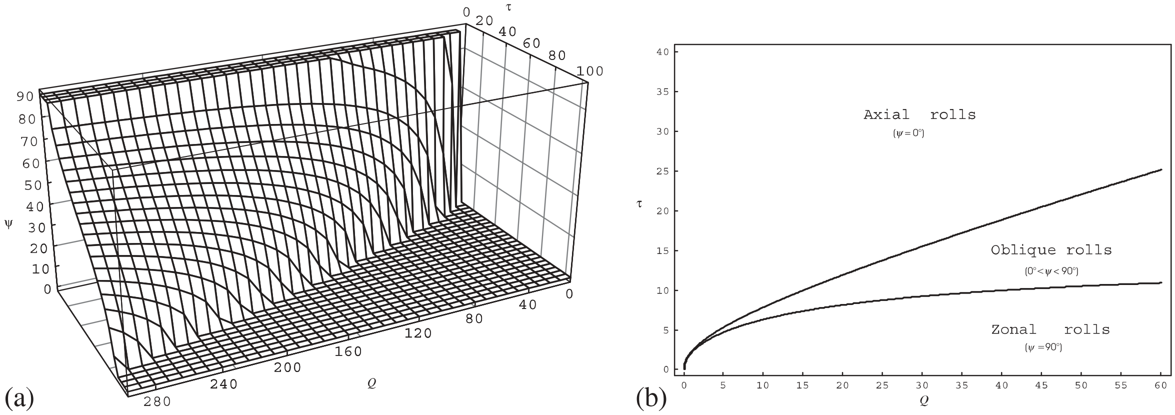

**Fig. 3.** (**a**) The obliqueness angles, $\psi$, of the critical wave vector $\boldsymbol{q}_c$ as a function of $\tau$ and $Q$. (**b**) The transition lines between zonal rolls, oblique rolls and axial rolls in the $Q$–$\tau$ plane (see text)

$R_c = 6417.048$, $|\boldsymbol{q}| = q = 1.9927$ and oblique angle, $\psi = 10.97°$ which compare well with the corresponding approximate values $R_c = 6459.938$, $q_c = 2.0022$ and $\psi = 13.34$.

## 4 Nonlinear analysis and instabilities

In order to assess the nature of the primary bifurcation to rolls we first perform the standard weakly nonlinear analysis in the vicinity of $R = R_c$. We solve Eq. (10) with the ansatz

$$\boldsymbol{V} = A\big(\exp[i\boldsymbol{q_c}\cdot\boldsymbol{x}]\boldsymbol{V_{lin}}(\boldsymbol{q_c}, z) + c.c.\ \big) + \boldsymbol{V}_\perp \tag{20}$$

where $c.c.$ indicates the complex conjugate and where $\boldsymbol{V}_\perp$ is of the order $\mathcal{O}(A^2)$ and orthogonal to the first term on the right hand side.

After expanding (10) in powers of $A$ and projecting on $\boldsymbol{V}_{lin}(\boldsymbol{q_c}, z)$ one arrives at the standard amplitude equation:

$$\frac{d}{dt}A = (\epsilon - \epsilon_c)A - cA^3 \tag{21}$$

with $\epsilon = (R - {R_c}^{RB})/{R_c}^{RB}$ and $\epsilon_c = (R_c - {R_c}^{RB})/{R_c}^{RB}$. We found exclusively supercritical (i.e. $c > 0$) bifurcations for values of the Prandtl number $P$ larger than unity.

In a further step, the stationary nonlinear roll solutions $\boldsymbol{V}_{roll}(\boldsymbol{x})$ for a given wave vector $\boldsymbol{q}$ are determined by solving the nonlinear coupled Eqs. (10) for the various expansion coefficients by the Newton–Raphson method. For this purpose the general representation (11) can be simplified by dropping the summation over $m$ for axial rolls and the summation over $l$ for zonal rolls. In the case of oblique rolls we assume $m = l$. The weakly nonlinear solutions are used to provide suitable starting values for the Galerkin calculations.

The stability of rolls is examined as usual by linearizing (10) about the Galerkin solutions $\boldsymbol{V}_{roll}$ using the ansatz

$$\boldsymbol{V}(\boldsymbol{x}, t) = \boldsymbol{V}_{roll}(\boldsymbol{x}) + \exp[\sigma_n t + i\boldsymbol{s}\cdot\boldsymbol{x}]\,\delta\boldsymbol{V}(\boldsymbol{x}) \tag{22}$$

with the Floquet wave vector $\boldsymbol{s} = (s_x, s_y, 0)$. Here $\delta\boldsymbol{V}(\boldsymbol{x})$ is a periodic function of $\boldsymbol{x}$ with the same spatial period as $\boldsymbol{V}_{roll}(\boldsymbol{x})$. We arrive thus at a linear eigenvalue problem for $\sigma_n(R, \boldsymbol{q}, \boldsymbol{s})$. The condition $\Re\{\sigma_n\} = 0$ determines the secondary bifurcations of the rolls.

A representative stability diagram for convection roll in the $\tau$–$\epsilon$ plane is given in Fig. 4. Here and in the following we restrict the attention to the case $Q = 14$, $P = 10$. The diagram shows the threshold curve (solid thick) from the conductive to the convective state as function of $\tau$. As already discussed in the previous section we find zonal rolls at small $\tau$ and axial rolls at larger $\tau$ separated by a regime of oblique rolls which is indicated by vertical dashes on the threshold curve at $\tau = 7.2$ and $\tau = 9.5$.

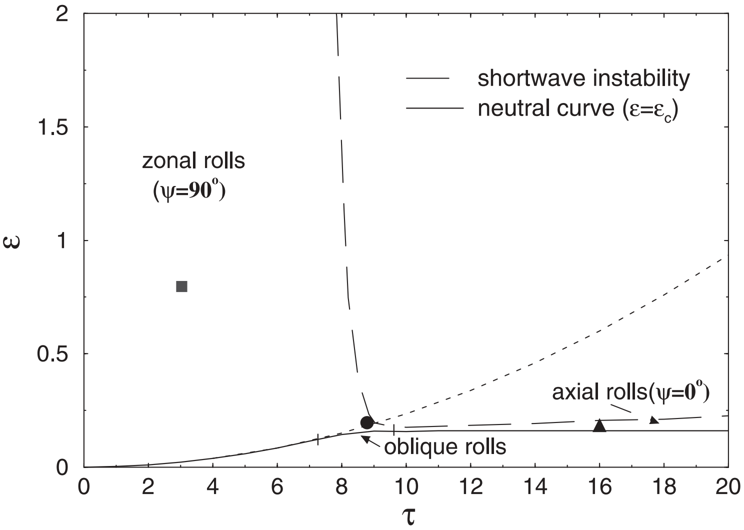

**Fig. 4.** Stability diagram for rolls with the critical wavevector $\boldsymbol{q_c}$ as a function of the rotation parameter $\tau$ for increasing $\epsilon$ in the case $Q = 14$, $P = 10$. The dotted curve indicates the neutral curve for zonal rolls and the black markers indicate the parameter values for which numerical simulation are described in Sect. 5

According to the stability diagram, rolls with the critical wavevector $\boldsymbol{q_c}$ are always found to be stable against long-wave perturbations ($|\boldsymbol{s}| \ll |\boldsymbol{q}|$). The zonal rolls at small $\tau \leq 7$ are stable against shortwave ($|\boldsymbol{s}| \approx |\boldsymbol{q}|$) instabilities as well. This is in contrast to the case of the axial rolls for large $\tau$, which become unstable at the dashed line in Fig. 4 by shortwave perturbations. For $\tau > 9$, the hexaroll instability (see e.g., in Auer et al. [2], Busse et al. [4]) comes into play, where $|\boldsymbol{s}| \cong |\boldsymbol{q}|$ and the angle between $\boldsymbol{s}$ and $\boldsymbol{q}$ approaches 60°.

The oblique rolls in the intermediate regime $7.2 < \tau < 9.5$ are stable below the dashed curve. The instability resembles the hexaroll instability although the angle of the disturbance differs from the value 60° assumed in the axial roll regime.

## 5 Numerical simulation of the evolution of convection in time

The results of the stability analysis presented in Fig. 4 are incomplete since roll solutions with a wavevector $\boldsymbol{q}$ different from the critical one $\boldsymbol{q_c}$ have not been considered. When this is done the results shown in Fig. 5 are obtained. For instance, the region of stable axial rolls is expanded since axial rolls with $q = 2.8$ turn out to be stable to higher values of $\epsilon$ than axial rolls with $q_c = 2.95$. Even more striking is the result that the region of stable zonal rolls is expanded to much higher values of $\tau$ as indicated by the dotted line in Fig. 5. The wavenumbers $q$ of the most stable zonal rolls are given by the numbers close to the curve.

The study of the stability of rolls by the Galerkin method has been complemented by the direct simulation method. The simulations are started either from random initial condition or from a roll pattern with a superimposed noise. In the latter case, we are able to confirm the stability boundaries of convection rolls obtained from the Galerkin code since the noise contribution decays with time in the stable roll regime. In Figs. 4 and 5, we have indicated some parameter values for which long period simulations have been done, which will now be discussed in detail.

As seen in Fig. 4, stable zonal rolls exist in the entire left side of the figure even for large $\epsilon$ values. This is confirmed by simulations started with random initial conditions. Indeed, as shown in Fig. 6, zonal roll structures perfectly aligned with the magnetic field are obtained after a relatively short time.

In the case of moderate $\tau$ values which are comparable to the value of $Q$, oblique rolls as predicted by linear analysis are found for low values of $\epsilon$. A typical time evolution from random initial conditions to an oblique roll pattern is shown in Fig. 7. The preferred angle of oblique rolls changes rapidly as $\epsilon$ is increased. This is evident from Fig. 5 where the approximate regions of stability of oblique rolls are indicated (thin lines). As the angle $\psi$ approaches 90° with increasing $\epsilon$, we enter the stability region of zonal rolls. This ten-

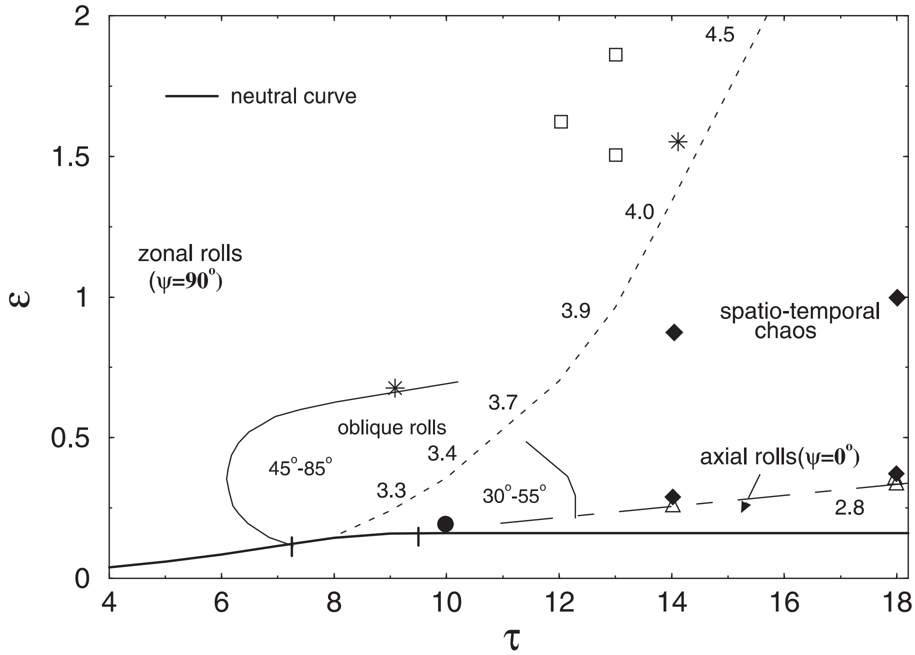

**Fig. 5.** Stability diagram and convection patterns in the $\tau$–$\epsilon$ plane in the case of $Q = 14$ and $P = 10$. Simulations discussed in the text have been done at the indicated points. Open squares indicate zig-zag patterns, open triangles correspond to knot patterns, closed diamonds indicate spatio-temporally chaotic convection and stars indicate the points where two different patterns have been obtained. The dotted curve determines the value of $\tau$ up to which stable steady zonal rolls with wavenumbers $q$ as indicated can be obtained. Stable axial rolls are found between the neutral curve and the dash-dotted line

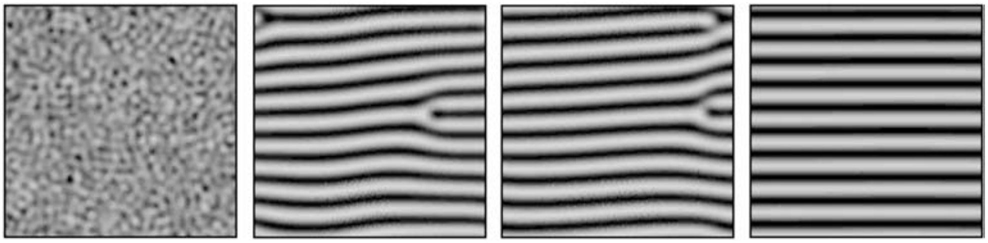

**Fig. 6.** Zonal rolls for $\tau = 3$, $\epsilon = 0.8$. The plots from left to right correspond to the times $t = 0$, 14.3, 28.57 and 114.3. The aspect ratio is $\Gamma = 20$. Here and in the following figures the temperature field in the plane $z = 0.5$ is shown. The $x$-coordinate increases towards the right and the $y$-coordinate is directed upwards

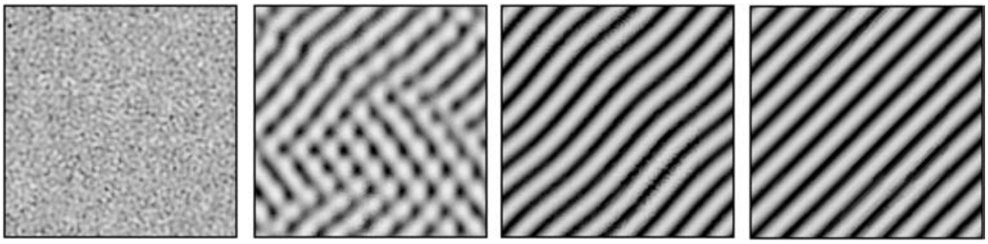

**Fig. 7.** Oblique rolls for $\tau = 8.7$, $\epsilon = 0.18$. The plots from left to right correspond to the times $t = 0$, 13.6, 27.3 and 109.1. The aspect ratio is $\Gamma = 20$

dency towards zonal rolls with increasing $\epsilon$ has also been observed experimentally (Jaletzky and Busse [9]) as well as theoretically (Busse et al. [4]) in the case $Q = 0$.

The range of stable zonal rolls above the dotted line in Fig. 5 overlaps to a considerable extent with the region where stable oblique rolls with the critical wavenumber $q_c$ are found. Accordingly we expect the hys-

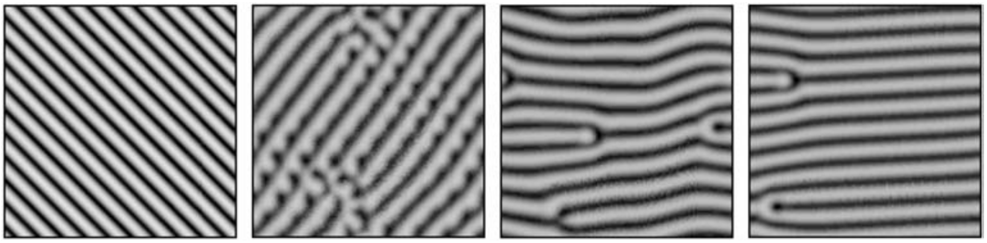

**Fig. 8.** The evolution of the convection pattern for $\tau = 9.1$, $\epsilon = 0.65$ starting from initial conditions of oblique rolls with superimposed noise. The plots from left to right correspond to the times $t = 7.1$, 32.9, 58.6 and 428.57. The aspect ratio is $\Gamma = 20$

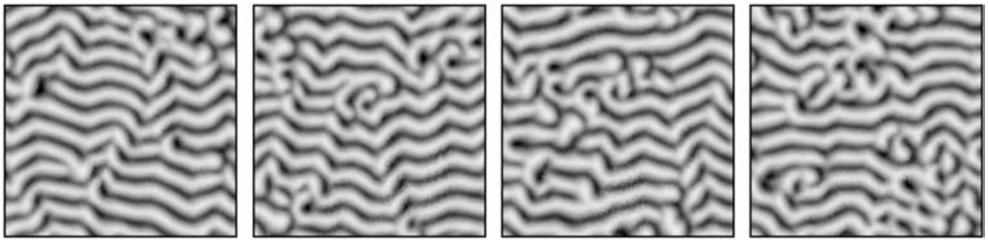

**Fig. 9.** The pattern evolution for the same parameters as in Fig. 8 starting from random initial conditions. The plots from left to right correspond to the times $t = 48.3$, 71.7, 113.3 and 466.7, respectively. The aspect ratio is $\Gamma = 20$

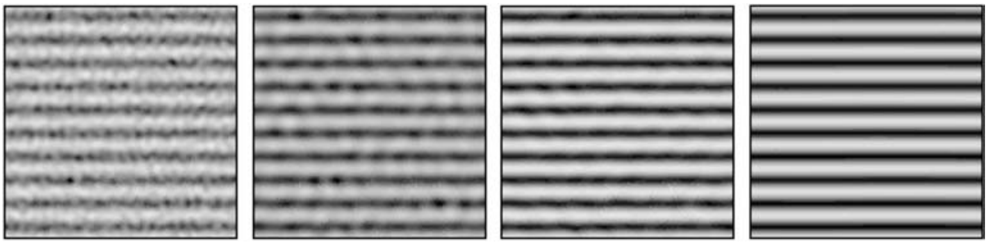

**Fig. 10.** Stable zonal rolls at the simulation point is denoted by a star in Fig. 5 for $\tau = 14$, $\epsilon = 1.54$, $q_{zonal} = 4$. The plots from left to right correspond to times $t = 0$, 0.125, 0.25 and 5. The aspect ratio is $\Gamma = 16$

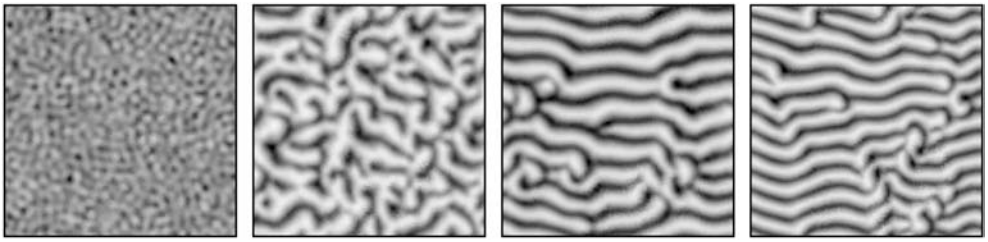

**Fig. 11.** Evolution of convection from random initial condition for the same parameters as in Fig. 10. The plots from left to right correspond to times $t = 0$, 1.7, 5 and 433. The aspect ratio is $\Gamma = 21$

teresis phenomena. Oblique rolls with increasing angle are found when $\epsilon$ is increased. But zonal rolls persist when $\epsilon$ is decreased down to the dotted line in Fig. 5.

To the right of the dashed line of Fig. 4 at values of $\epsilon$ of the order unity it depends on the initial condition whether stable zonal rolls are realized or not. This property is demonstrated in Fig. 8 where initially oblique rolls evolve into a pattern of zonal rolls with two dislocations which are likely to disappear after much longer integration times. In contrast, when the integration in time is started with random initial conditions a steady pattern of zonal rolls will not be obtained as asymptotic state. Instead a spatio-temporally chaotic pattern persists in which zonal rolls predominate only locally as demonstrated in Fig. 9. The coex-

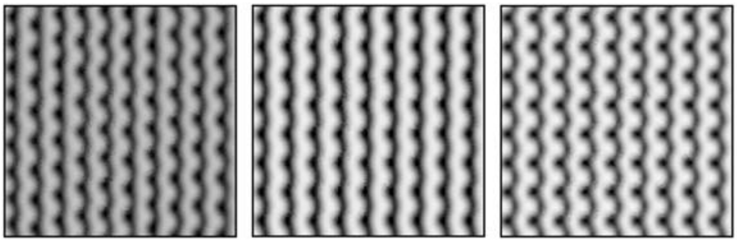

**Fig. 12.** Stable knot convection patterns for $\tau = 14$, $\epsilon = 0.247$ (left plot), $\tau = 18$, $\epsilon = 0.326$ (middle plot) and $\tau = 18$, $\epsilon = 0.342$ (right plot). The aspect ratio is $\Gamma = 22$

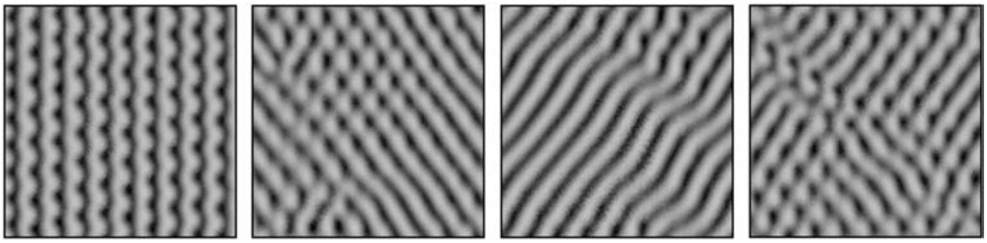

**Fig. 13.** Evolution of spatio-temporally chaotic oblique rolls for $\tau = 14$, $\epsilon = 0.28$. Corresponding times are $t = 33.3$, 50, 83.3 and 150, respectively. The aspect ratio is $\Gamma = 20$

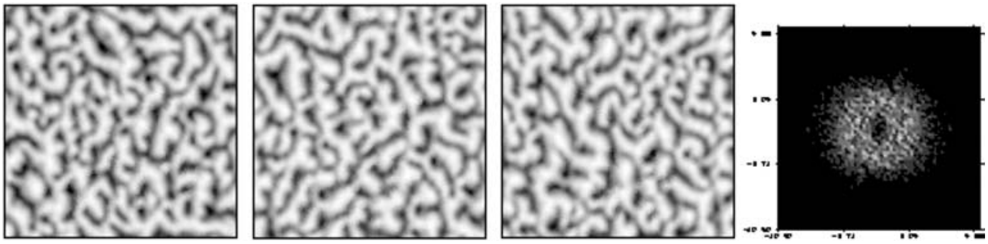

**Fig. 14.** Spatio-temporal pattern for $\tau = 18$, $\epsilon = 1$. Last picture gives the power spectrum of the last pattern. The plots from left to right correspond to times $t = 8.3$, 16.7 and 25. The aspect ratio is $\Gamma = 20$

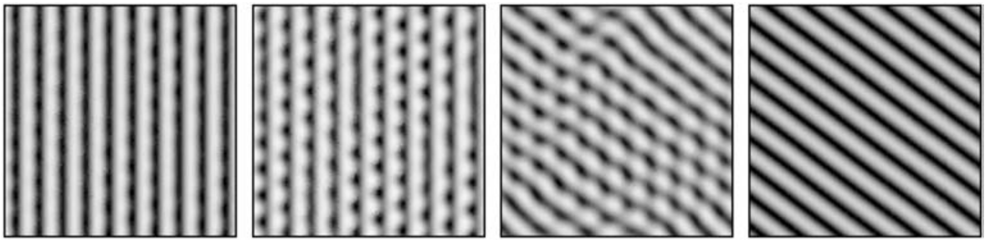

**Fig. 15.** Stable oblique rolls just above the instability line for $\tau = 10$, $\epsilon = 0.19$. The plots from left to right correspond to times $t = 5.5$, 6.4, 18.2 and 327.3. The aspect ratio is $\Gamma = 20$

istence of steady attractors and spatio-temporally chaotic ones is a well known phenomenon in problems of pattern formation. For an example we refer to the case of spiral defect chaos in RB convection (Cakmur et al. [5]). Another example of this phenomenon is demonstrated by Figs. 10 and 11 for a much higher value of $\tau$.

The stability region of axial rolls remains relatively small even when wavenumbers $q$ other than the critical value are considered. Beyond the stability boundary stable steady knot convection is realized in the cases $\tau = 14$ and $\tau = 18$ for a small interval of $\epsilon$ as shown in Fig. 12. At slightly higher value of $\epsilon$ a chaotic pattern is found which is dominated by a switching back and forth between the two kinds of oblique rolls with an angle of $\psi = \pm 37°$ as shown in Fig. 13. For even larger values of $\epsilon$ the oblique rolls are replaced by fully

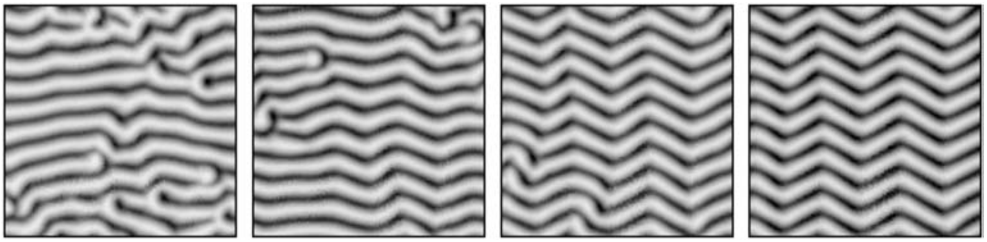

**Fig. 16.** Zig-zag pattern evolving from random initial condition for $\tau = 13$, $\epsilon = 1.51$. The plots from left to right correspond to the times $t = 5$, 33.3, 66.6 and 100. The aspect ratio is $\Gamma = 20$

phase-turbulent convection in this regime. An example is shown in Fig. 14. We have included a graph of the power spectrum which corresponds to the last spatial pattern in Fig. 14. Note that the ring like wave vector distribution is nearly isotropic with the approximate mean radius given by $| \boldsymbol{q}_c |$. This feature can be understood on the basis of the property that the stabilizing effects exerted by rotation and by the magnetic field in the two orthogonal directions are approximately equal.

For lower values of $\tau$ the axial rolls become unstable to the hexaroll instability according to the Galerkin analysis. But instead of a steady hexaroll pattern the convection evolves into a stable oblique roll pattern in agreement with the stability results. This evolution is shown in Fig. 15. Note that hexaroll instability is well expressed in the transients.

In a region surrounding the open squares in Fig. 5 steady zig zag patterns have been found as attractors as shown, for example, in Fig. 16. Outside this region, however, spatio-temporally chaotic convection is usually found when the simulations are started with random initial conditions.

## 6 Concluding remarks

Although only a small part of the parameter space of convection in a rotating cylindrical annulus has yet been investigated, it is obvious from the results of this paper that a large variety of spatio-temporal patterns can be found in this problem. It will be of interest to obtain a comparison with experimental observation eventually. Because of the geophysical and astrophysical relevance of the problem some experimental attempts towards a laboratory realization of this convection problem have been made. Brito and Cardin [3] have experimentally realized convection in an annular configuration with an azimuthal magnetic field in liquid sodium. Because of the low viscosity of this liquid metal they had to use high values of the Coriolis parameter $\tau$ in order to achieve a centrifugal force exceeding gravity by a sufficiently high factor. The high value of $\tau$ in their experiment prevented them to attain a value of $Q$ comparable to that of $\tau$, which appears to be necessary to obtain convection structures deviating from the axial roll structure.

Low values of $\tau$ in centrifugally driven convection can be realized when high Prandtl number fluids are used as in the experiments of Jaletzky and Busse [9]. Unfortunately high Prandtl number liquids usually do not offer high electrical conductivities which facilitate the attainment of sufficiently high values of $Q$. However, high Prandtl number electrolytes could eventually solve this experimental problem. An experiment on the RB convection in an electrolyte with a horizontal magnetic field without rotation has recently been performed by Andreev et al. [1].

## References

1. Andreev, O., Haberstroh, C., Thess, A.: Visualisation of magnetoconvection. Phys. Fluids **15**, 3886–3889 (2003)
2. Auer, M., Busse, F.H., Clever, R.M.: Three-dimensional convection driven by centrifugal buoyancy. J. Fluid Mech. **301**, 371–382 (1995)
3. Brito, D., Cardin, P.: private communication (2003)
4. Busse, F.H., Zaks, M.A., Brausch, O.: Centrifugally driven thermal convection at High Prandtl Numbers. Physica D **184**, 3–20 (2003)
5. Cakmur, R.V., Egolf, D.A., Plapp, B.B., Bodenschatz, E.: Bistability and competition of spatiotemporal chaotic and fixed point attractors in Rayleigh–Bénard convection. Phys. Rev. Lett. **79**, 1853–1856 (1997)
6. Chandrasekhar, S.: *Hydrodynamics and Hydromagnetic Stability*. Oxford Uni. Press, London (1961)

7. Eltayeb, I.A.: Hydromagnetic convection in a rapidly rotating fluid layer. Proc. R. Soc. Lond. A **326**, 229–254 (1972)
8. Eltayeb, I.A.: Overstable hydromagnetic convection in a rapidly rotating fluid layer. J. Fluid Mech. **71**(1), 161–179 (1975)
9. Jaletzky, M., Busse, F.H.: New patterns in centrifugally driven thermal convection. Proc. Nat. Acad. Sci. **97**, 5060–5064 (2000)
10. Pesch, W.: Complex spatiotemporal convection patterns. Chaos **6**(3), 348–357 (1996)